

pubs.acs.org/crystal Article

# Highly Polymorphous Nicotinamide and Isonicotinamide: Solution versus Melt Crystallization

Published as part of a Crystal Growth and Design virtual special issue in Celebration of the Career of Roger Davey

Noalle Fellah, Carolyn Jin Zhang, Catherine Chen, Chunhua T. Hu, Bart Kahr, Michael D. Ward, and Alexander G. Shtukenberg\*



Cite This: Cryst. Growth Des. 2021, 21, 4713–4724



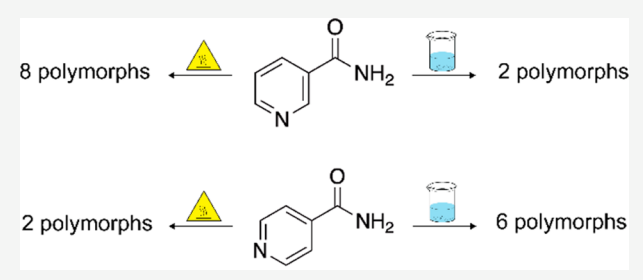
ACCESS

III Metrics & More

Article Recommendations

Supporting Information

ABSTRACT: The crystallization of nicotinamide (NA) and its constitutional isomer, isonicotinamide (INA), is compared. NA formed eight polymorphs from the melt and two from solution, whereas INA formed two polymorphs from the melt and six from solution. This analysis was provoked by the observation that NA is highly polymorphic from the melt, while the closely related INA is highly polymorphous from solution. A combination of hot stage polarized light microscopy, powder X-ray diffraction, and Raman spectroscopy revealed that the polymorph selectivities are not related to supramolecular self-association in the growth media. The larger



estimated free energy gap separating NA polymorphs, compared with that of the INA polymorphs, is consistent with the smaller number of NA polymorphs generated from solution. Phenomenological analyses of crystallization kinetics suggest that cross nucleation is the most likely reason more polymorphs of NA than INA crystallize from the melt.

# ■ INTRODUCTION

Molecular crystals feature shallow free energy landscapes with multiple shallow minima corresponding to different polymorphs differing by less than a few kJ/mol at room temperature. This can cause anxiety for those whose fortunes depend on deterministic crystallizations, especially compounds where purity, thermal stability, crystal habit, bioavailability, or emerging properties are major considerations. Unfortunately, reliable strategies for controlling polymorph selectivity are rare, and a practitioner's guide for controlling polymorphism is wanting. Davey, Cruz-Cabeza, and Feeder reflected on this problem: <sup>1</sup>

"In theory, one would want to generate the polymorphic landscape of a compound computationally, link it to crystal properties, retrieve the crystallization conditions of the desired form and crystallize it. In practice, computationally generated polymorphic landscapes are challenging, structure—property relationships are not yet accurately predictable, we rarely design crystallization conditions for the discovery of specific polymorphic forms and crystallization process design remains a challenging engineering exercise."

Among the outstanding issues is a dearth of kinetic data linking forms to crystallization conditions. Davey, among others, has relied on the predictive value of solution associations.  $^{2-10}$  Direct comparison of polymorph crystallization kinetics can also guide outcomes from melts,  $^{11,12}$  albeit

each compound has idiosyncrasies that thwart generalization. Few studies have addressed the influence of the crystallization medium on the outcomes. Clarifying this influence may inform Price's question derived from her experience with crystal structure prediction: "Why don't we find more polymorphs?" <sup>13</sup>

Herein, we analyze connections between crystallization pathways and polymorphism of nicotinamide (NA) and isonicotinamide (INA), constitutional isomers that differ only in the relative position of the heteroatom and substituent (Scheme 1). Solubilities (Table S1) and thermochemical properties are similar;<sup>14</sup> yet, these compounds crystallize quite

Scheme 1. Nicotinamide (NA) and Isonicotinamide (INA)

**Received:** May 10, 2021 **Revised:** July 6, 2021 **Published:** July 21, 2021





differently. NA forms eight polymorphs from the melt<sup>15–18</sup> but only two from solution.<sup>19–22</sup> INA, in contrast, has been reported to form six polymorphs from solution<sup>22–25</sup> but none from the melt. Here we ask: Why is the crystallization for these two isomers so different? Which factors play a role in these crystallization outcomes? We evaluate herein three possible explanations: (i) polymorph accessibility across free energy landscapes, (ii) molecular self-association in the growth medium, and (iii) differences in crystallization kinetics.

NA and INA are among a class of pyridine carboxamides widely used in medicinal chemistry. NA is a precursor of vitamin B<sub>3</sub> used for the treatment of nutritional deficiencies and diabetes. 26-28 INA is a popular cocrystal former with active pharmaceutical ingredients (APIs), 23,29,30 and it has recently been investigated for anti-inflammatory activity and treatment of Huntington's disease. 31,32 The rich polymorphism of NA from the melt was first reported by Kofler and Kofler in 1943, who used optical microscopy to identify six different polycrystalline spherulites. 15 In 1971, Kolfer and Kolšek amended the melting temperatures and morphologies of the six forms and reported the discovery of a seventh polymorph. 16 A report contemporaneous with our investigation gave singlecrystal structures of all seven known NA polymorphs as well as two new ones, 18 also obtained by melt crystallization. This work highlighted the versatility of melt crystallization for polymorph discovery, especially within regions of the potential energy landscape inaccessible by solution crystallization or in cases where theoretical predictions are limited (i.e., for Z' > 2structures). As described below, we have observed all NA polymorphs except NA VI. Unfortunately, the discovery of polymorphs across decades has produced inconsistent nomenclatures. While Greek letters have been introduced recently for designating NA polymorphs, 18 Roman numerals were used originally by Kofler and Kofler. We use the Roman designations herein, but we list the polymorphs with both conventions, as well as their corresponding melting temperatures, in Table S2. The crystal structures of NA I and II were determined for single crystals grown in solution, 19,21,21,22 and the structures of the remaining polymorphs were determined for single crystals grown by melt crystallization. 18 The nine single-crystal structures of NA are available in the Cambridge Structure Database (CSD).

Six polymorphs of INA, I–VI, have been grown from solutions, and their structures have been solved by single-crystal X-ray diffraction (SCXRD).<sup>22–25</sup> INA V has been reported to crystallize only in the presence of substituted 3-arylbutanoic acids.<sup>24</sup> To our knowledge, INA polymorphs from the melt have not been reported previously.

## **■ EXPERIMENTAL SECTION**

**Materials.** NA (purity >99.5%) and INA (purity 99%) were purchased from Sigma-Aldrich (St. Louis, Missouri) and used without further purification. All solvents were reagent grade.

**Melt Crystallization.** 3–5 mg of NA (mp = 129 °C) and INA (mp = 158 °C) were melted between two glass coverslips on a Kofler bench (film thickness was 4–7  $\mu$ m). The samples were subsequently cooled on the Kofler bench or by quenching to room temperature (20–24 °C) by placing the melted samples onto an aluminum block acting as a heat sink. Some samples of INA were prepared as mixtures with natural resins (10–30 wt %), such as damar gum, or below room temperature (ca. 0 °C) by quenching the sample with dry ice. Growth and nucleation of NA and INA crystalline phases from the melt were observed by polarized light microscopy using a hot stage (model FP90, Mettler-Toledo) with the temperature regulated between 30

and 129 °C. In most experiments, a constant temperature was achieved within 15 s. Polarized light micrographs were made with Olympus BX50 and BX53 microscopes equipped with digital cameras. Growth and nucleation kinetics of NA between room temperature and the melting point, and growth kinetics of INA within the temperature range of 150-156 °C, were measured using polarized light microscopy, with the temperature controlled by the hot stage. Linear growth rates, V, were measured as the displacement of the growth front divided by the elapsed time. Nucleation rates, I, were estimated for the samples rapidly cooled to a specific temperature as the number of nuclei per area of the sample per crystallization time. If nucleation occurred too quickly such that it was hard to count the number of nuclei even after 20 s, the nucleation rate was estimated from the time needed for complete crystallization,  $\tau$ , and the average size of spherulites achieved after full crystallization, L, using a geometric condition for 2D crystallization,  $I = 1/(L^2\tau)$ . Because of the rapid crystallization of INA, it could not be cooled below 150 °C in a hot stage without complete crystallization, and approximate growth and nucleation rates are given. INA was first melted on a Kofler bench and then rapidly moved along the bench to the target temperature in less than 5 s. The nucleation and growth rates were then calculated from the total time of crystallization,  $\tau$ , and the average size of spherulites, L, as  $I = 1/(L^2\tau)$  and  $V = L/(2\tau)$ .

**Solution Crystallization.** Crystallization of NA and INA from solution was performed by either cooling supersaturated solutions or by solvent evaporation. The former was performed by preparing a supersaturated solution of NA or INA in a closed vial at  $55-90\,^{\circ}$ C, followed by cooling to  $25\,^{\circ}$ C at a rate of  $5\,^{\circ}$ C/h using a crystallization incubator (EchoTherm, Torrey Pines Scientific Inc., Carlsbad, California), after which the solution was allowed to stand at  $25\,^{\circ}$ C overnight. NA or INA were dissolved in a closed vial on a hot plate at  $30-40\,^{\circ}$ C ( $T_{\rm dissolv}$ ). The solution was kept at  $T_{\rm dissolv}$  for  $5\,^{\circ}$ min and then removed from the hot plate. The vial cap was removed, and the solvent was allowed to evaporate under ambient conditions.

**X-ray Diffraction.** Two-dimensional powder X-ray diffraction (2D PXRD) was performed with a Bruker D8 Discover General Area Detector Diffraction System (GADDS) equipped with a VÅNTEC-2000 2D detector and Cu-K $\alpha$  source ( $\lambda$  = 1.54178 Å), monochromated with a graphite crystal and collimated with a 0.5 mm capillary collimator (MONOCAP). Data collection of melt crystallized samples was performed in the reflection mode on an asgrown crystalline film on a cover glass (top glass removed) or in the transmission mode on a Kapton 0.8 mm capillary loaded with powder that had been scraped carefully with a needle from a crystalline film on a glass slide. Crystals grown from solution were removed from the mother liquid and ground into a fine powder. The powder was loaded into a Kapton 0.8 mm capillary.

Single-crystal X-ray diffraction data sets were recorded on a Bruker D8 APEX-II CCD system with the  $\omega$  scans at 100 K using graphite-monochromated and 0.5 mm MonoCap-collimated Mo-K $\alpha$  radiation ( $\lambda$  = 0.71073 Å). Structures were solved by intrinsic phasing methods (SHELXT), and the models were refined using the full-matrix least-squares on  $F^2$ . Single cocrystals of NA and formamide were grown from formamide solution by cooling, while single cocrystals of NA and acetic acid, as well as INA monohydrate, were grown from acetic acid and aqueous solutions, respectively, by evaporation. Crystallographic information files (CIFs), including the HKL and RES data, are deposited in the Cambridge Crystallographic Data Centre (CCDC) with Nos. 2082164, 2082165, and 2082166.

**Raman Spectroscopy.** Raman spectra were collected with a Raman microscope (DXR, Thermo Fisher Scientific, Waltham, MA) using a 532 nm excitation laser operating at 8 mW, high-resolution grating, 2 cm<sup>-1</sup> resolution,  $\sim$  2  $\mu$ m spatial resolution, and a 50  $\mu$ m slit width. The data were analyzed with the OMNIC software.

Differential Scanning Calorimetry (DSC). DSC measurements were performed on a PerkinElmer DSC 8000 under nitrogen gas purge. Bulk powders of INA and NA were hermetically sealed in aluminum pans and heated at a rate of  $10~^{\circ}\text{C/min}$  for heat of fusion measurements and  $60~^{\circ}\text{C/min}$  for heat capacity measurements.

INA samples were heated to 200  $^{\circ}$ C, and NA samples were heated to 140  $^{\circ}$ C. The data were analyzed using PerkinElmer software.

**Free Energy Calculation.** The free energy difference between melt at the melting point,  $T_{\rm m}$ , and a given polymorph at temperature T was estimated using eq 1. $^{33,34}$ 

$$\begin{split} \Delta G_{\rm V} &= \frac{\Delta H(T_{\rm m}-T)}{T_{\rm m}} - \int_{T}^{T_{\rm m}} \left(C_{p\rm L}-C_{p\rm C}\right) \, {\rm d}T' \\ &+ T \int_{T}^{T_{\rm m}} \frac{\left(C_{p\rm L}-C_{p\rm C}\right)}{T'} \, {\rm d}T' \end{split} \tag{1}$$

Here,  $\Delta H$  is heat of fusion and  $C_{p\mathrm{C}}$  and  $C_{p\mathrm{L}}$  are heat capacities at constant pressure for a given polymorph and melt, respectively. Because of the low kinetic stability of some NA and INA polymorphs, eq 1 was applied only for NA I, NA II, NA III, NA IV, INA I, INA II, INA III, and INA IV, for which heat of fusion and heat capacities could be measured from DSC scans. A simplified expression for the driving force of crystallization (eq 2) was also used to compare all polymorphs, using the assumption that  $C_{p\mathrm{L}}-C_{p\mathrm{C}}=0$ .

$$\Delta G_{\rm V} = \frac{\Delta H(T_{\rm m} - T)}{T_{\rm m}} \tag{2}$$

In solution, the magnitude of  $\Delta G_V$  reflects the difference between solution concentration, c, and solubility,  $c_{\rm eq}$ , for a given polymorph (eq 3) where R is the universal gas constant.

$$\Delta G_{\rm V} = RT \ln \left( \frac{c}{c_{\rm eq}} \right) \tag{3}$$

**Surface Energy Calculation.** Average surface energy values of NA and INA polymorphs were calculated based on the growth morphology method using the Morphology module in Materials Studio (Materials Studio 18.1.0.202, Accelrys, San Diego, CA). The crystal structures for all NA and INA polymorphs were obtained from CIFs deposited in the CCDC and optimized using the COMPASS II force field. Geometry optimizations were conducted using the Forcite tool. The Ewald summation method was chosen for the evaluation of van der Waals and electrostatic terms.

# RESULTS AND DISCUSSION

**Melt Crystallization.** Polymorphs were initially identified from their crystal morphologies as observed with a polarized light optical microscope. The data were then corroborated and confirmed by Raman microscopy and PXRD. The temperature ranges for the crystallization of the NA polymorphs from the melt are summarized in Figure 1 and Table 1. The data are largely consistent with previous reported results. <sup>18</sup> Nucleation and growth of NA I were observed throughout the temperature (T) range, and it was the only form observed at T > 117 °C,

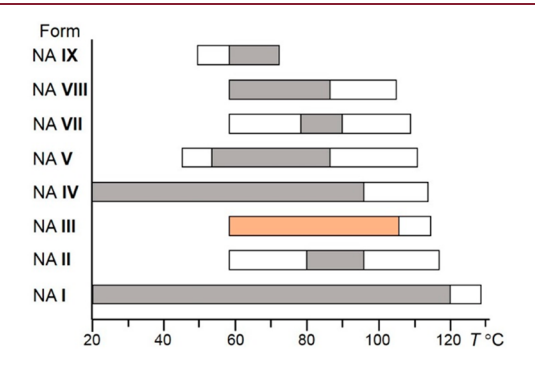


**Figure 1.** Temperature ranges of NA crystallization. Color scheme: Gray = nucleation and growth; white = growth on seeds; orange = nucleation within NA IV spherulites.

Table 1. Melting Points of NA Polymorphs

NA polymorph	T <sub>m</sub> , °C	$\Delta G^a$ , kJ mol <sup>-1</sup>	$\Delta G^b$ , kJ mol <sup>-1</sup>	$c_{\mathrm{eq},i}/c_{\mathrm{eq},\mathrm{I}}^{c}$	$c_{\mathrm{eq},i}/c_{\mathrm{eq},\mathrm{I}}^{}d}$
I	128.9(1)	0	0	1	1
II	115.9(2)	0.89	0.75	1.43	1.35
III	114.5(2)	0.87	0.83	1.42	1.40
IV	112.6(2)	0.70	0.94	1.33	1.46
$\mathbf{v}$	110.6(2)	n/d <sup>f</sup>	1.06	n/d	1.53
VII	108.7(3)	n/d	1.17	n/d	1.60
VIII	104.5(5)	n/d	1.41	n/d	1.77
IX	103 <sup>e</sup>	n/d	1.50	n/d	1.83

<sup>a</sup>Free energy difference between the liquid phase and polymorph i and NA I was obtained with eq 1. <sup>b</sup>Free energy difference between polymorph i and NA I was obtained with eq 2 with the heat of fusion for NA I of  $\Delta H_{\rm I} = 23.3$  kJ/mol. <sup>c,d</sup>The ratio between solubilities of polymorph i and NA I was calculated with eq 3 using  $\Delta G$  obtained from eq 1 (c) and eq 2 (d); T = 298 K. <sup>e</sup>Melting point of NA IX was taken from ref 18. <sup>f</sup>n/d = not determined.

where nucleation was extremely slow (<1 event/cm²/h). NA I at lower temperatures (T < 117 °C), however, grew fast and covered most of the slide as opaque spherulites with a fibrous texture and first-order interference colors (Figure 2A,B).

NA II crystallized spontaneously at 70–85 °C as coarse spherulites with small linear birefringence (Figure 2C). NA II also appeared as a transformation product from NA VIII, forming irregular, coarse spherulites<sup>35</sup> (Figure 2D). NA III crystallized spontaneously above 60 °C, apparently as a transformation product of NA IV, forming block-shaped single crystals with first- to second-order interference colors<sup>36</sup> (Figure 2E).

NA IV was observed most commonly, nucleating spontaneously at T < 95 °C. This polymorph dominated at T < 55 °C and demonstrated a wide range of growth morphologies (Figure 2A-G,I,J). At T > 70 °C, NA IV formed opaque spherulites with first- to second-order interference colors. Its morphology was like that of NA I, with micron-sized fibers (Figure 2B) that thickened (tens of microns) above 85 °C (Figure 2F). As T decreased to 65 °C, coarse spherulites of NA IV transformed into fine spherulites containing submicron fibers that exhibited gray to black interference colors (Figure 2F). At T < 60 °C, differently oriented fibrous needles with first- to second-order interference colors began to dominate, eventually forming fine spherulites with micron-sized fibers and second- to third-order interference colors (Figure 2F). This morphology persisted up to 75 °C, although it constituted only a small fraction of NA IV above 55 °C. NA V spontaneously crystallized as spherulites with high (typically third order) interference colors at 55-85 °C (Figure 2G). NA VII presented with fine spherulites between 80 and 90 °C, which exhibited banded morphologies characteristic of rhythmic twisting, 37,38 as well as nonbanded morphologies (Figure 2H,I). Banding was observed above 85 °C. NA VIII dominated from 65 to 75 °C, forming spherulites with needle-like and plank-like orientations of crystallites, exhibiting first- to second-order interference colors (Figure 2A,D,J). Below 65 °C, NA II, VII, and VIII transformed to NA IV via cross nucleation (Figure 2C,I,J). NA IX was a minor form, spontaneously crystallizing from the melt near 70 °C as low birefringent (gray to yellow interference colors) spherulites (Figure 2J). Below 50 °C, NA IX was highly unstable, converting to NA I via cross nucleation (Figure 2J) within 1 h and sometimes within minutes, even if crystallized between

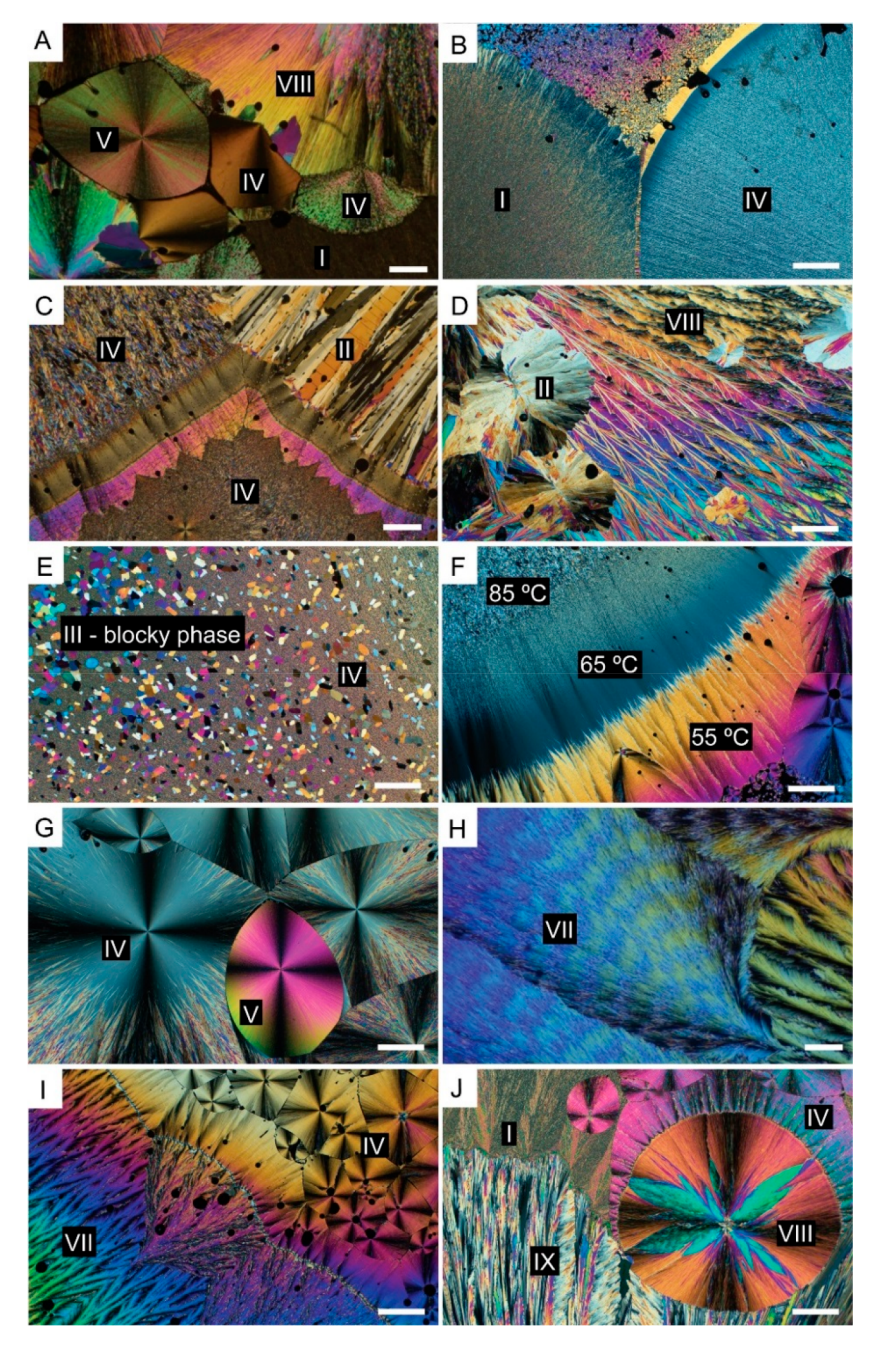


**Figure 2.** Polarized light micrographs of NA polymorphs from the melt. (A) NA **I**, **IV**, **V**, and **VIII** concomitantly nucleated and grew ca. 60 °C. (B) NA **I** and NA **IV** crystallizing at ca. 80 °C. (C) Spherulites of NA **II** and **IV** nucleated at 80–85 °C. As the temperature was decreased, the morphology of NA **IV** exhibited a series of morphological changes, while NA **II** converted to NA **IV** via cross nucleation. (D) NA **VIII** grown at ca. 70 °C with transformation product NA **II**. (E) NA **III** crystallized at ca. 60 °C as blocks inside NA **IV**. (F) Evolution of NA **IV** growth as temperature was lowered. A coarse spherulite grew at 85 °C, with thinner fibers emerging when the sample was moved to the 65 °C zone on the Kofler bench and differently oriented fibers when moved to 55 °C. (G) NA **V** crystallized at ca. 65 °C, surrounded by NA **IV**. (H) Banded spherulite of NA **VII** formed at 85 °C with the nonbanded region of the same form. (I) Cross nucleation of NA **VIII** → NA **IV** at 80 °C. (J) Cross nucleation of NA **VIII** → NA **IV**, and NA **IX** → NA **I** at 45 °C. Scale bar = 200 μm for all images except (G), for which it is 50 μm.

glass slides. NA IX was reported to crystallize easily from the melt seeded with INA. The room temperature (ca. 23 °C), metastable polymorphs NA II through V, VII, and VIII transformed into stable NA I within a few days if between glass slides or in hours to minutes if powdered. NA VI (named form  $\zeta$  elsewhere, Table S2) was not observed in our melt experiments.

Measurement of melting points,  $T_{\rm m}$ , using differential scanning calorimetry (DSC) was not possible for several of

the metastable forms due to the rapid polymorph transformation to NA I upon heating. Consequently, the melting points were marked by the movement of the melt–crystal interface using a polarized light microscope equipped with a hot stage. The measured melting points (Table 1) agree with previous findings. The phase transformations indicated monotropic relationships across the entire temperature range above room temperature. Free energy differences between the polymorphs were estimated using  $T_{\rm m}$  and the heat of fusion of

NA I measured by DSC,  $\Delta H = 23.3$  kJ/mol (Table 1). All NA polymorphs were distinguishable by Raman spectroscopy (Figure S1) and PXRD.

INA crystallized more simply from the melt. INA II, the thermodynamically stable form at high temperatures, at least above 120  $^{\circ}$ C, was observed throughout the T range studied. INA II formed large centimeter-sized crystals above 150  $^{\circ}$ C (Figure 3A) and coarse spherulites at lower temperatures

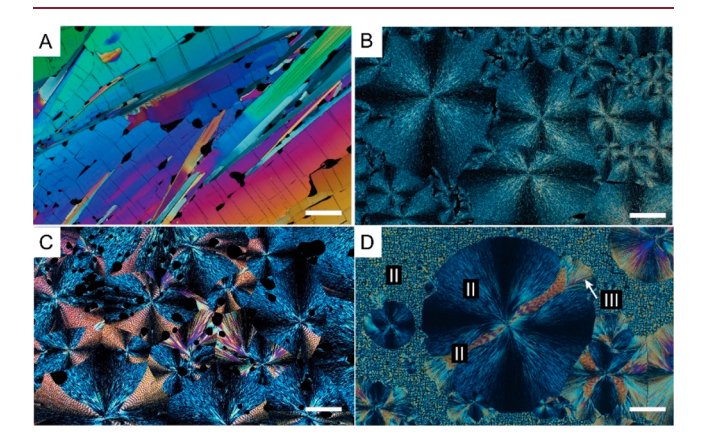


**Figure 3.** Polarized light micrographs of INA polymorphs from the melt. (A) Crystals of INA **II** grown at 155 °C. (B) Coarse spherulites of INA **II** formed at ca. 60–90 °C. (C) INA **II** grown at 40 °C in the presence of damar gum (ca. 15 wt %). (D) INA **II** and **III** crystallized at room temperature (ca. 20 °C) with damar gum. INA **II** appeared in all regions, except the nonbanded region of high birefringence which corresponded to INA **III**. Scale bars:  $(A-C) = 200 \ \mu m$ ; (D) =  $50 \ \mu m$ .

(Figure 3B). With damar gum (ca. 15 wt %) at T < 50 °C and without additives below room temperature, spherulites of INA II covered large regions with first- to second-order interference colors and out-of-phase zig-zagging banding, as well as with smaller regions of slightly higher interference colors and circular bands (Figure 3C). A small fraction of fine spherulites, INA III by Raman spectroscopy, with slightly higher interference colors were identified (Figure 3D).

 $T_{\rm m}$  was measured on a hot stage (Table 2). Crystals grown in solution were used for the  $T_{\rm m}$  measurements of INA I, III, and IV, while INA II was crystallized from the melt. The fast transformation of INA VI upon heating precluded its  $T_{\rm m}$  determination. We were also not able to obtain INA V. After several weeks at ambient conditions, some samples of INA II began transforming to INA I, indicating an enantiotropic

Table 2. Melting Points of INA Polymorphs

INA polymorph	T <sub>m</sub> , °C	$\Delta G^a$ , kJ mol <sup>-1</sup>	$\Delta G^{b}$ , kJ mol <sup>-1</sup>	$c_{\mathrm{eq},i}/c_{\mathrm{eq},\mathrm{I}}^{c}$	$c_{\mathrm{eq},i}/c_{\mathrm{eq},\mathrm{II}}^{}d}$
I	148.3(3)	-0.32	0.52	1	1.23
II	157.6(1)	0	0	1.14	1
III	148.5(3)	0.37	0.51	1.32	1.23
IV	154.5(3)	0.09	0.17	1.18	1.07

"Free energy difference between the liquid phase and polymorph i and INA II was obtained with eq 1. "Free energy difference between polymorph i and INA II was obtained with eq 2 with the heat of fusion for INA II is  $\Delta H_{\rm II} = 24.3$  kJ/mol. ""The ratio between solubilities of polymorph i and INA I (c) and INA II (d) was calculated with eq 3 using  $\Delta G$  obtained from eq 1 (c) and eq 2 (d); crystallization temperature T = 298 K. Melting points were not determined for INA V and VI.

relationship, wherein INA I transforms to INA II near 123 °C. The free energy rankings between the polymorphs were estimated using  $T_{\rm m}$  and the heat of fusion of INA II ( $\Delta H = 24.3 \text{ kJ/mol}$ ) measured by DSC (Table 2).

Solution Crystallization. Solution crystallization screenings were performed in common organic solvents (Table S3). Previous reports of NA crystallization from solution claimed the formation of the thermodynamically stable NA I, as needles. 19-21 Single crystals of NA II from solution were later reported but only in the presence of isoxyl (also known as thiocarlide;  $N,N'-[4-(3-methylbutoxy)-phenyl]thiourea).^{22}$ Here, solution screens with pure solvents (by cooling or evaporation) eschewed additives or templates.<sup>39</sup> All solvents, except acetic acid and formamide, produced needles of NA I. Large blocks were grown by evaporation of acetic acid solutions, corresponding to an NA-acetic acid 1:2 cocrystal not reported previously (CCDC No. 2082164). The cocrystal was unstable in air and transformed to NA I upon the loss of acetic acid. Cooling of formamide solution resulted in NAformamide 1:1 cocrystal, also not previously reported (CCDC No. 2082165). In one instance, NA VII crystallized from dichloromethane, but this result could not be reproduced. INA I, II, III, IV, and VI crystallized from a range of solvents, frequently concomitantly. INA, like NA, formed cocrystals, as reported previously, with acetic acid (REFCODE: JAW-WAG)<sup>40</sup> and formamide (REFCODE: GAVHER),<sup>41</sup> as well as a monohydrate from isopropanol and water solutions. The structure of the monohydrate is reported here (CCDC No. 2082166).

Factors Controlling Polymorph Selection. We first considered kinetic and thermodynamic factors driving polymorph selection. A polymorph (i = 1, 2, ...N) can be observed only if its fraction in the solid mixture,  $x_{ij}$  is above a detection threshold, which for routine optical and PXRD measurements is  $x_i > 10^{-2}$  (1%). Under favorable crystallization conditions, wherein crystals obtained by cooling from the melt range from 20 to 50  $\mu$ m, optical microscopy can detect much smaller fractions, as low as  $x_i > 10^{-5}$ . A polymorph also needs to be sufficiently stable for detection. This typically is not problematic for melt crystallization between two glass slides, as transformation can be detected using a polarized light microscope, even if the polymorph lifetimes are only a few seconds. The value of  $x_i$  for thin films can be calculated from the Avrami equation for multicomponent systems (eq 4a),<sup>42</sup> where  $J_i$  and  $V_i$  are nucleation  $[1/m^2/s]$  and growth [m/s]rates, respectively. The approximation in eq 4a is applicable if a small fraction of some polymorph,  $x_i < 0.05$ , is determined with respect to a dominant polymorph (a common occurrence also applicable to NA and INA).

$$x_{i} = \frac{J_{i}V_{i}^{2}}{\sum_{j=1}^{N}J_{j}V_{j}^{2}} \approx \frac{J_{i}V_{i}^{2}}{J_{\text{major}}V_{\text{major}}^{2}}$$
 (4a)

Crystallization from solution typically requires longer times than from the melt (hours and days vs. seconds and minutes), and polymorph conversion can be overlooked easily due to rapid solvent-mediated phase transformations. The value of  $x_i$  can be obtained from eq 4b, which also accounts for the 3D geometry of the medium, with a nucleation rate now expressed in proper units  $[1/\text{m}^3/\text{s}]$ .

$$x_{i} = \frac{J_{i}V_{i}^{3}}{\sum_{j=1}^{N}J_{j}V_{j}^{3}} \approx \frac{J_{i}V_{i}^{3}}{J_{\text{major}}V_{\text{major}}^{3}}$$
(4b)

Equations 4a and 4b predict that the polymorph fractions will be governed by the relationships between corresponding growth and nucleation rates. According to classical nucleation theory, the rate of nucleation can be written as eq 5, where  $J_0$  is a constant that varies minimally with temperature and growth conditions and is not polymorph dependent,  $\Delta G_{\rm D}$  is the activation free energy for a molecule to transfer from the growth medium to a nucleus,  $\Delta G^*$  is the thermodynamic barrier for nucleation,  $\gamma$  is the crystall-medium interface energy,  $\omega$  is the molar volume, and  $\Delta G_{\rm V}$  is the driving force for crystallization. 33

$$J = J_0 \exp\left(-\frac{\Delta G_D + \Delta G^*}{RT}\right)$$

$$= J_0 \exp\left(-\frac{\Delta G_D}{RT}\right) \exp\left(-\frac{16\pi}{3} \frac{\gamma^3 \omega^2}{RT \Delta G_V^2}\right)$$
(5)

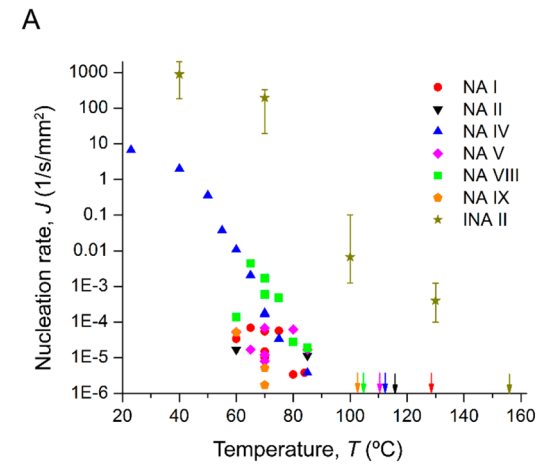
The  $\Delta G_{\rm V}$  term can be expressed as eqs 1 and 2. The corresponding growth rate can be calculated using eq 6,<sup>43</sup> where  $V_0$  is a polymorph-independent constant.

$$V = V_0 \exp\left(-\frac{\Delta G_{\rm D}}{RT}\right) \left[1 - \exp\left(-\frac{\Delta G_{\rm V}}{RT}\right)\right]$$
(6)

The differences between I and V among different polymorphs are governed primarily by differences in  $T_{\rm m}$ ,  $\Delta H$ ,  $\gamma$ ,  $\omega$ , and  $\Delta G_D$ . The kinetic barriers for nucleation and growth (the first exponential terms in eqs 5 and 6, respectively) are expected to be similar, as recently confirmed in a study of the melt crystallization of polyalcohols.<sup>44</sup> In the case of crystallization from the melt, small differences in  $T_{\rm m}$ ,  $\Delta H$ ,  $\gamma$ , and  $\omega$  among polymorphs can have a profound effect on J and V near the melting point. Nucleation rates close to the melting point, however, are typically negligible (Figure 4A), whereas at lower temperatures, nucleation becomes detectable (Figure 4A). The growth rates among different polymorphs are typically comparable, varying within 1-1.5 orders of magnitude 45,46 (Figure 4B) because the second exponential in eq 6 tends to zero, while the first exponential, related to the melt viscosity, does not vary significantly. Thus, at sufficiently high supercooling, (i) the driving force ( $\Delta G_V$  in eqs 1 and 2) is large enough for all polymorphs; (ii) the kinetic barrier for growth and nucleation ( $\Delta G_D$  in eqs 5 and 6) is comparable for different polymorphs; (iii) the nucleation rate is controlled by the differences in  $\Delta G^*$  in eq 5.

In solution, nucleation commences closer to equilibrium than melt crystallization due to smaller crystal—solution interface energies and faster mass transport. Therefore, maintaining a stable supersaturated solution with respect to the least stable polymorphs can be difficult. Solutions that are highly supersaturated with respect to the more stable forms are often only slightly supersaturated with respect to the least stable form. Once a more stable polymorph nucleates, the supersaturation of the solution rapidly decreases, preventing further nucleation.

Moreover, crystallization from solution is more sensitive to differences in growth rates than from the melt (eq 4b), as  $\Delta G_D$  is more variable. Consequently, compared to melt crystallization, polymorph screening from solution is hampered by (i)



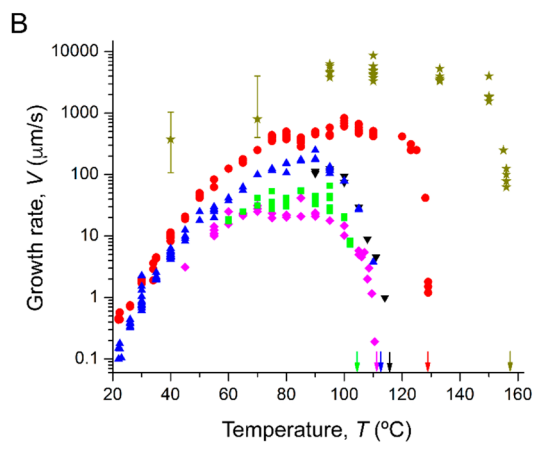


**Figure 4.** Dependence of (A) nucleation and (B) growth rates of NA I, II, IV, V, VIII, IX, and INA II polymorphs from the melt on growth temperature. The values of J and V for INA at  $T < 100\,^{\circ}\mathrm{C}$  have significant errors due to the inability to reach the target temperatures before the crystallization starts. Arrows highlight melting points of corresponding polymorphs. If not shown, the error bars are comparable with the symbol size.

the difficulty in creating a sufficiently high crystallization driving force for all polymorphs; (ii) the dominance of faster-growing polymorphs; (iii) the disparate effects on the kinetic barrier for crystallization in various solvents compared with compositionally unchanging melt.

In sum, NA and INA grow quite differently from melt and solution. Eight of nine NA polymorphs crystallized from the melt without additives, and only one of nine polymorphs consistently appeared in crystallization from solution. On the other hand, only two of six INA polymorphs crystallized from the melt, and five of the six crystallized readily from various solvents. Below, we explore the likely reasons for such differences, including (i) differences in driving force for crystallization; (ii) differences in the kinetic barrier for crystallization; and (iii) the interplay between growth and nucleation kinetics.

**Energy Landscape.** Metastable polymorphs have higher free energies,  $G_V$ , compared with the thermodynamically stable polymorph, i.e., higher solubilities and lower melting points. During crystallization from the melt, supercooling (the driving force for crystallization) with respect to all polymorphs is easily achieved because the rate of sample cooling is typically much faster than the rate of crystallization. The melting point ranges

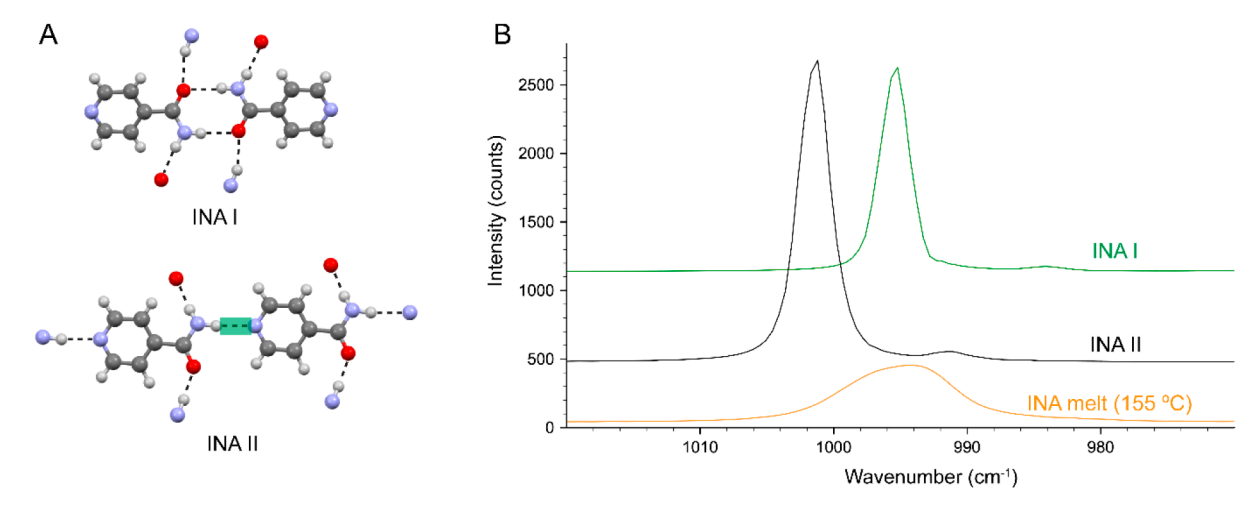


Figure 5. (A) Hydrogen-bonding motifs for INA I (top) and INA II (bottom). The (pyridine)N···H—N hydrogen bond in INA II is highlighted in green. (B) Raman spectra of INA I (green), INA II (black), and an INA melt at 155 °C (orange).

for NA and INA polymorphs span 26 and 10 °C, respectively (Tables 1 and 2), and crystallization for both compounds is facile for supercooling ( $\Delta T = T_{\rm m} - T$ ) up to 100 °C (Figure 4). Thus, all polymorphs of NA and INA can be accessed from the melt.

Compared to melt crystallization, nucleation from solution begins at low supersaturation. Solubility ratios,  $c_{\rm eq}$ ,  $c_$ (Tables 1 and 2), between the metastable NA and INA polymorphs, i, and their respective thermodynamically stable polymorphs (NA I and INA II, respectively) can be estimated from eq 3, using the free energy differences calculated with eqs 1 and 2 (Experimental Section). The free energy differences between NA polymorphs obtained from eq 1 are consistent with those obtained from eq 2. This demonstrates that the formation of even the second-most stable form, NA II, requires at least  $c/c_{eq.I} > 1.35$ , a high supersaturation that is difficult to obtain and maintain; the least stable polymorph, NA IX, requires  $c/c_{eq,I} > 1.83$  (Table 1). A similar analysis for INA is slightly more complex due to the experimentally observed enantiotropic relationship between INA I and INA II, while eq 2 always assumes monotropic phase relationships. The free energy differences calculated using eq 1 indeed are consistent with the enantiotropic relationship between INA I and INA II. Nonetheless, both estimates, eqs 1 and 2, reveal a smaller span of free energies among the INA structures compared to NA structures. For example, according to eq 1, INA I is the most stable polymorph at room temperature, and  $c/c_{eq.I}$  ranges from 1.14 for INA II to 1.32 for INA III, whereas according to eq 2, INA II is the most stable polymorph at room temperature, and  $c/c_{eq,II}$  ranges from 1.07 for INA IV to 1.23 for INA I (Table 2). Collectively, the data are consistent with INA polymorphs being much more energetically accessible compared with NA polymorphs. Indeed, we observed that INA I, II, III, and IV crystallized from various solvents, often concomitantly, while the same solvents produce NA I exclusively (Table S3). The energy landscape, as constructed above, favors multiple INA polymorphs and only one NA polymorph from solution. This is consistent with the experiment.

**Self-Association in Growth Media.** Attempts to characterize structural precursors during crystallization from melts are rare.<sup>47</sup> Over the past two decades, however, investigations have aimed to link solute—solute and solute—solvent interactions with polymorphic outcomes. Such

interactions can alter the kinetic barrier for nucleation and growth,  $\Delta G_{\rm D}$  (eqs 5 and 6), resulting in drastically different nucleation and growth rates for different polymorphs, with some much less likely to crystallize. Spectroscopic assays of supramolecular solute associations have been compared with the final crystal structure. This approach has provided plausible evidence for the preservation of solute—solute associates, consistent with a deterministic role of the solvent in the crystallization outcome.  $^{2-4,48-50}$  Other studies, however, have not found such connections, citing alternative explanations.  $^{6,7,51,52}$ 

Spectroscopic assays have been applied to INA as well. Raman and FTIR spectroscopy gave evidence of head-to-head dimers between amide groups in solvents with strong hydrogen bond donors, such as isopropanol, methanol, and ethanol.<sup>53</sup> This led to the formation of INA I, which is the only INA crystal structure to contain the hydrogen-bonded dimer motif (Figure 5A, Table S4). Conversely, solvents with strong hydrogen bond acceptors led to head-to-tail chains ((pyridine)-N···H-N) as the dominant configuration observed in INA II-VI (Figure 5A, Table S4). These head-to-tail chains are absent in the INA I structure. These observations led to the conclusion that the hydrogen-bonding configurations play a key role in the nucleation kinetics of their respective polymorph, 33 providing an appealing framework for understanding the crystallization of nicotinamide isomers. Even so, the crystallization outcomes from our investigation contradict these observations (Table S3). Strong hydrogen bond donors, such as isopropanol, methanol, and ethanol, were expected to favor the formation of the dimer motif, and thus the crystallization of INA I.53 However, under the same cooling crystallization conditions, 53 INA I crystallized concomitantly with INA II, III, and IV (Table S3). Similarly, strong H-bond accepting solvents, such as nitromethane, yielded INA I instead of the previously reported INA II.53 Notably, different polymorphic outcomes depended on the crystallization conditions. In the case of nitromethane, INA II and IV were observed by evaporation crystallization, while INA I was obtained by controlled cooling with the same solvent. INA precipitation from ionic liquids is likewise inconsistent with a direct solution-structure link.54

Self-association does not justify the crystallization of NA. For example, head-to-head dimers between amide groups are

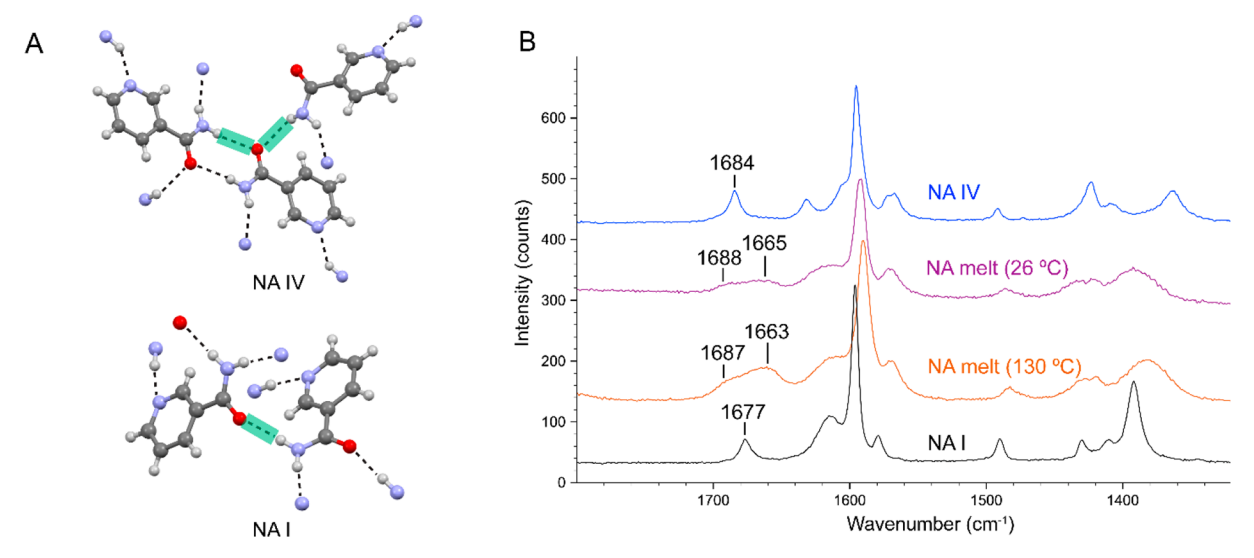


Figure 6. (A) Hydrogen-bonding motifs for NA IV (top) and I (bottom). The N-H···O hydrogen bonds in both structures are highlighted in green. (B) Raman spectra of NA IV (blue), NA I (black), NA melt at 26 °C (purple), and NA melt at 130 °C (orange).

observed in NA IX as well as NA I (Table S5), but NA I crystallized consistently, regardless of solvent. This argues that self-association in solution does not explain the solution polymorphism of NA.

The role of intermolecular associations in the melt crystallization outcomes was analyzed with Raman spectroscopy. In the case of INA, Raman spectra were acquired for the melt at 155 °C, just prior to crystallization of INA II, using the ring breathing mode of the pyridine moiety<sup>55</sup> as a metric for (pyridine)N···H-N hydrogen bonding. In the melt, this mode is observed as a broad peak at 994 cm<sup>-1</sup>, comparable to INA I (995 cm<sup>-1</sup>), but INA II exhibits this mode at 1001 cm<sup>-1</sup> (Figure 5B). The higher wavenumber is consistent with pyridine nitrogen coordination<sup>56</sup> due to the formation of the (pyridine)N...H-N hydrogen bond in the head-to-tail chain motif observed in INA II (green highlight in Figure 5A). This hydrogen bond motif does not exist in INA I (Figure 5A) and is reflected by the lower value of 995 cm<sup>-1</sup> for the ring breathing mode. The equi-energetics of the ring breathing modes for the INA melt and INA I (994 cm<sup>-1</sup> vs 995 cm<sup>-</sup> respectively) obviates head-to-tail chain association in the melt. Consequently, the Raman data suggest no link between intermolecular associations in the INA melt and INA II, the predominant crystalline phase (Table S4), as from solution.

As described above, all polymorphs of NA can be obtained within a narrow temperature range, 75 °C < T < 90 °C. Below 60 °C, nucleation and growth of NA IV are preferred, while above 90 °C, NA I dominates (Figure 1). Reasonably, intermolecular associations in a melt of NA at room temperature, prior to crystallization, reflect those observed in NA IV, whereas a melt at 130 °C exhibits associations reflecting those in solid NA I. The crystal structures of the NA polymorphs (Table S5) are characterized by complex sets of hydrogen bonds, especially the high Z' structures. Both NA I and IV exhibit head-to-tail chain configurations; therefore, the pyridine ring breathing mode is an unsuitable metric for differentiating intermolecular associations. Instead, the hydrogen-bonding configurations of the NA melt and crystals are better assessed using the carbonyl vibrational stretching mode,  $^{57}$   $v_{C=0}$  near 1680 cm<sup>-1</sup> (Figure 6). Assignments of the peaks shown in Figure 6 appear in Table S6. The carbonyl

oxygen participates in only one N–H···O bond in the NA I structure and corresponds to a peak at 1677 cm<sup>-1</sup>, whereas the carbonyl oxygen in NA IV is associated with two independent N–H···O bonds and appears as a peak at 1684 cm<sup>-1</sup>.

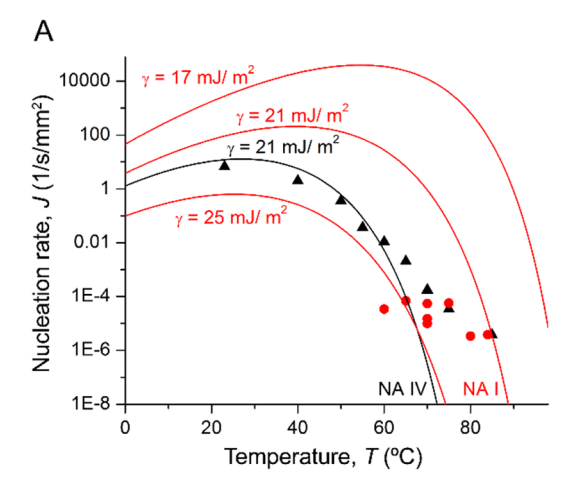
Unlike the solid forms of NA, the melt spectra contained additional peaks assignable to the  $\nu_{\text{C=O}}$  stretching mode, suggesting the presence of varied associations. Consequently, the molecular associations at 130 and 26 °C do not directly signify the crystallization outcome of NA I or IV. Spectra of NA melts at 70 °C, 80 °C, and 90 °C do not change across the entire temperature range of NA crystallization (Figure S3). Once again, crystallization from the melt cannot be attributed to intermolecular associations in the melt with confidence.

**Crystallization Kinetics from the Melt.** Although the melt can provide a high crystallization driving force, only two of the six INA polymorphs were observed in this way. Several kinetic mechanisms may account for this difference.

Differences in Polymorph Detection Limits. Since INA nucleates and grows much faster than NA (Figure 4), the latter has more time for the crystallization of multiple polymorphs. This expectation is misleading. Equation 4a predicts that the minimum detectable fraction of polymorph, *i*, depends on the ratio of growth and nucleation rates, not on their absolute values. Moreover, the presence of inert resins, such as damar gum or Canada balsam in amounts ranging from 10 to 30%, slows crystallization of INA by as much as two orders of magnitude. This is comparable to the growth and nucleation rates of NA, but the polymorph outcome does not change. Thus, smaller absolute growth and nucleation rates do not lead directly to a larger number of observed polymorphs.

Differences in  $\Delta G^*$ . Small differences in polymorph melting points  $(T_{\rm m})$ , surface energies  $(\gamma)$ , and heats of fusion  $(\Delta H)$  can produce significant differences in the thermodynamic barrier for nucleation  $(\Delta G^*)$ . This can lead to substantial changes in the nucleation rate because of its exponential dependence on the free energy terms in eq 5. The nonlinear dependence of nucleation rates of forms at a given temperature may depend on the aforementioned thermodynamic quantities. The nucleation rates for NA polymorphs were measurable over a relatively narrow temperature range (Figure 1) compared with NA I and IV.

Nucleation rates of NA IV were simulated using eq 5, with the molar volume  $\omega = 8.5 \times 10^{-5} \, \mathrm{m}^3/\mathrm{mol}$  and heat of fusion  $\Delta H = 23.3 \, \mathrm{kJ/mol}$ . The value of  $\Delta G_\mathrm{D} = 150 \, \mathrm{kJ/mol}$  was determined by fitting experimentally measured growth rates far from the melting point with eq 6 (Figure S4). The preexponential factor,  $J_0$ , and crystal-melt interfacial energy,  $\gamma$ , were used as fitting parameters. A reasonable fit to the experimental data (Figure 7A) was obtained with  $\gamma =$ 



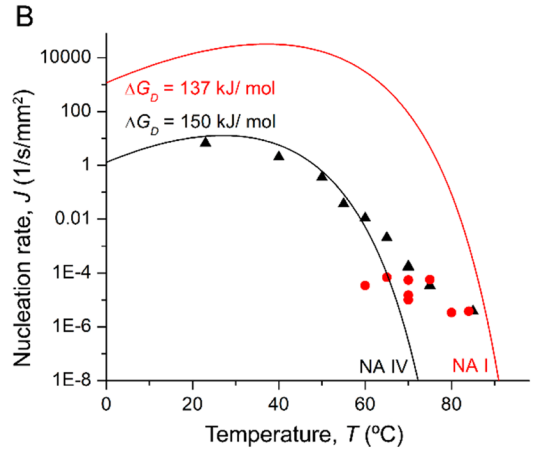


Figure 7. Dependence of measured nucleation rates of NA I (red circles) and IV (black triangles) on crystallization temperature. The lines represent fits using eq 5 for various values of (A) surface energy  $\gamma$ , with  $\Delta G_{\rm D}=150$  kJ/mol, and (B) two different values of  $\Delta G_{\rm D}$ , obtained from growth rate data in Figure S4, with  $\gamma=21$  mJ/m². The fits in both (A) and (B) assume  $J_0=4\times10^{31}$  1/s/mm².

21 mJ/m² (Table S7). The discrepancy between the fit and experimental data may be related to errors in measuring small nucleation rates. This fit can be used to estimate the effect of  $T_{\rm m}$ ,  $\Delta H$ , and  $\gamma$  on the thermodynamic term  $\exp(-\Delta G^*/RT)$  in eq 5. First, we simulated J(T) for the same set of parameters with melting points corresponding to NA IV and I. The ratio of nucleation rates  $J_{\rm NA(IV)}/J_{\rm NA(I)}$  rapidly approaches unity with decreasing temperature (Figure 7A). Variations of crystal-melt interface energy,  $\gamma$ , among polymorphs are not significant, typically not exceeding 20–30%<sup>58</sup> (Tables S7, S8). Simulations performed with  $\gamma$  = 17, 21, and 25 mJ/m² demonstrate that the nucleation rates of NA I and IV become comparable at lower temperatures, specifically within two orders of magnitude (Figure 7A). Moreover, because the surface energy is proportional to the heat of fusion, eqs 2 and 5 predict that  $\gamma$ 

 $\propto \Delta H^{59}$  and  $\Delta G^* \propto \gamma^{-3}/\Delta H^2$ , and the overall effect of variations in  $\Delta H$  and  $\gamma$  on  $\Delta G^*$  should be even smaller. Compared with NA, the melting points of INA polymorphs are higher, the differences between them are smaller, the calculated surface energies differ less (Table S8), and the values of  $\Delta H$  and  $\omega$  are even more similar. Consequently, a smaller difference in the  $\Delta G^*$  values for INA polymorphs is expected with high supercooling, which would favor a larger number of INA polymorphs from the melt. This expectation, however, is contrary to our observations.

Differences in  $\Delta G_D$ . As discussed above, the values of  $\Delta G_D$  are associated with the molecular mobility in the melt and are expected to be similar for all polymorphs. Fitting NA growth rates far from the melting point with eq 6 afforded  $\Delta G_D = 137(3)$  and 150(3) kJ/mol for NA I and IV, respectively (Figure S4), resulting in a larger difference in the calculated nucleation rates (Figure 7B). The actual difference in  $\Delta G_D$  may be even smaller, as  $\Delta G_D = 145(3)$  and 146(3) kJ/mol can be obtained from the fit for NA I and NA IV, respectively, if the data at 22 °C, where the rate measurements are less reliable, are excluded. Compared with NA,  $\Delta G_D$  values for different INA polymorphs should be more similar because of their higher  $T_{\rm m}$ 's. Consequently, one would expect that most INA polymorphs should be observed, but they are not.

Cross nucleation. Cross nucleation describes the heterogeneous nucleation of a kinetically favorable polymorph on the surface of the kinetically less favorable one. 11,12,45,60-62 The probability of cross nucleation increases as the driving force for crystallization (i.e., supercooling) increases. If cross nucleation occurs on a parent crystal with submicron dimensions, the new polymorph may not be detected, which can explain the fewer than expected number of melt-crystallized polymorphs at high supercooling. Cross nucleation plays an important role in NA melt crystallization. Indeed, at 70 °C, nucleation rates of NA IV and VIII are comparable. Meanwhile, at 60 °C, the nucleation rate of NA IV increases, but the nucleation rate of NA VIII decreases (Figure 4A), with most NA VIII spherulites eventually forming NA IV on their growth fronts via cross nucleation (Figure 2]). At lower temperatures, NA VIII does not form even though the difference in growth and nucleation rates should decrease as temperature decreases. The spherulites of NA II and VII stop growing below 60 °C; NA IV nucleates on their surfaces and grows instead (Figure 2C,I). Below 50 °C, NA IX is replaced by NA I through cross nucleation (Figure 2J). Thus, cross nucleation seems to be responsible for the dramatic decrease of the number of spontaneously nucleating NA polymorphs as the temperature decreases from 70 to 80 °C to 20-40 °C (Figure 1). Hypothetically, if cross nucleation became faster at 60-80 °C, we would likely see only one or two NA polymorphs from the

INA II strongly dominates crystallization from the melt. INA melts were seeded with different INA polymorphs (ca. 20 individual experiments for each polymorph) and monitored by polarized light microscopy. Seeding of INA melts with INA I and INA IV results in only INA II growth. INA III nucleates independently near room temperature but not at higher temperatures. Seeding an INA melt with INA III above 80 °C generated INA II primarily, likely from cross nucleation; INA III was obtained in only one of ca. 20 attempts. Thus, cross nucleation seems to be an important mechanism for INA melt crystallization. Even if other polymorphs nucleated, they would

transform immediately to INA II via cross nucleation, escaping detection.

## CONCLUSIONS

Isomers NA and INA are highly polymorphic materials that, nevertheless, express their polymorphism under different circumstances. Eight of nine NA polymorphs easily nucleate from the melt, and only one of nine consistently appears in crystallization from solution. Meanwhile, only two of six INA polymorphs directly nucleate from the melt, but five of six forms can easily crystallize from solution.

The observations suggest that the polymorph selectivities in solution and melt for NA and INA are not related to supramolecular association in the growth medium. The puzzle presented by the distinct crystallization phenomena of the isomers can be explained by a smaller span of free energies among the INA structures compared to NA structures, which favors crystallization of INA from solution. It is difficult to reconcile the differences in crystallization from the melt, however. The larger number of NA polymorphs from the melt is not directly related to (i) the absolute values of growth and nucleation rates, (ii) the thermodynamic barrier for nucleation, or (iii) the kinetic barrier for nucleation and growth. Instead, the difference likely stems from different cross nucleation rates of NA and INA, which allows many NA polymorphs to be detected in a narrow temperature range.

# ASSOCIATED CONTENT

# **Supporting Information**

The Supporting Information is available free of charge at https://pubs.acs.org/doi/10.1021/acs.cgd.1c00547.

Solubility of nicotinamide and isonicotinamide, comparison of nicotinamide polymorphs, results of solution screening for nicotinamide and isonicotinamide, hydrogen-bonding motifs in nicotinamide and isonicotinamide, Raman spectra of nicotinamide and isonicotinamide polymorphs, nicotinamide melt, assignment of Raman spectra for nicotinamide, growth rates of nicotinamide polymorphs, calculated lattice and surface energies of nicotinamide and isonicotinamide polymorphs (PDF)

# **Accession Codes**

CCDC 2082164–2082166 contain the supplementary crystallographic data for this paper. These data can be obtained free of charge via www.ccdc.cam.ac.uk/data\_request/cif, or by emailing data\_request@ccdc.cam.ac.uk, or by contacting The Cambridge Crystallographic Data Centre, 12 Union Road, Cambridge CB2 1EZ, UK; fax: +44 1223 336033.

## AUTHOR INFORMATION

## **Corresponding Author**

Alexander G. Shtukenberg — Department of Chemistry and Molecular Design Institute, New York University, New York City, New York 10003, United States; orcid.org/0000-0002-5590-4758; Email: shtukenberg@mail.ru

#### **Authors**

Noalle Fellah — Department of Chemistry and Molecular Design Institute, New York University, New York City, New York 10003, United States

- Carolyn Jin Zhang Department of Chemistry and Molecular Design Institute, New York University, New York City, New York 10003, United States
- Catherine Chen Department of Chemistry and Molecular Design Institute, New York University, New York City, New York 10003, United States
- Chunhua T. Hu Department of Chemistry and Molecular Design Institute, New York University, New York City, New York 10003, United States; orcid.org/0000-0002-8172-2202.
- Bart Kahr Department of Chemistry and Molecular Design Institute, New York University, New York City, New York 10003, United States; orcid.org/0000-0002-7005-4464
- Michael D. Ward Department of Chemistry and Molecular Design Institute, New York University, New York City, New York 10003, United States; orcid.org/0000-0002-2090-781X

Complete contact information is available at: https://pubs.acs.org/10.1021/acs.cgd.1c00547

# Notes

The authors declare no competing financial interest.

#### ACKNOWLEDGMENTS

This work was supported primarily by the MRSEC Program of the National Science Foundation under Award Number DMR-1420073. It was also supported by the National Science Foundation under Award Number DMR-1708716. The X-ray microdiffractometer with GADDS was acquired through the support of the National Science Foundation under Award Number CRIF/CHE-0840277 and the NSF MRSEC Program under Award Number DMR-0820341.

# **■** REFERENCES

- (1) Cruz-Cabeza, A. J.; Feeder, N.; Davey, R. J. Open questions in organic crystal polymorphism. *Commun. Chem.* **2020**, *3*, 142.
- (2) Davey, R. J.; Blagden, N.; Righini, S.; Alison, H.; Quayle, M. J.; Fuller, S. Crystal polymorphism as a probe for molecular self-assembly during nucleation from solutions: the case of 2,6-dihydroxybenzoic acid. *Cryst. Growth Des.* **2001**, *1*, 59–65.
- (3) Parveen, S.; Davey, R. J.; Dent, G.; Pritchard, R. G. Linking solution chemistry to crystal nucleation: the case of tetrolic acid. *Chem. Commun.* **2005**, 1531–1533.
- (4) Musumeci, D.; Hunter, C. A.; McCabe, J. F. Solvent effects on acridine polymorphism. *Cryst. Growth Des.* **2010**, *10*, 1661–1664.
- (5) Mattei, A.; Li, T. Polymorph formation and nucleation mechanism of tolfenamic acid in solution: an investigation of prenucleation solute association. *Pharm. Res.* **2012**, *29*, 460–470.
- (6) Du, W.; Cruz-Cabeza, A. J.; Woutersen, S.; Davey, R. J.; Yin, Q. Can the study of self-assembly in solution lead to a good model for the nucleation pathway? The case of tolfenamic acid. *Chem. Sci.* **2015**, *6*, 3515–3524.
- (7) Tang, W.; Mo, H.; Zhang, M.; Parkin, S.; Gong, J.; Wang, J.; Li, T. Persistent Self-Association of Solute Molecules in Solution. *J. Phys. Chem. B* **2017**, *121*, 10118–10124.
- (8) Ischenko, V.; Englert, U.; Jansen, M. Conformational dimorphism of 1,1,3,3,5,5-hexachloro-1,3,5-trigermacyclohexane: Solvent-induced crystallization of a metastable polymorph containing boat-shaped molecules. *Chem. Eur. J.* **2005**, *11*, 1375–1383.
- (9) Shi, P.; Xu, S.; Ma, Y.; Tang, W.; Zhang, F.; Wang, J.; Gong, J. Probing the structural pathway of conformational polymorph nucleation by comparing a series of  $\alpha$ , $\omega$ -alkanedicarboxylic acids. *IUCrJ* **2020**, 7, 422–433.
- (10) Bobrovs, R.; Drunka, L.; Auzins, A. A.; Jaudzems, K.; Salvalaglio, M. Polymorph-selective role of hydrogen bonding and

- $\pi$ – $\pi$  stacking in *p*-aminobenzoic acid solutions. *Cryst. Growth Des.* **2021**, 21, 436–448.
- (11) Yu, L. Survival of the fittest polymorph: how fast nucleater can lose to fast grower. *CrystEngComm* **2007**, *9*, 847–851.
- (12) Yu, L. Polymorphism in molecular solids: an extraordinary system of red, orange, and yellow crystals. *Acc. Chem. Res.* **2010**, *43*, 1257–1266.
- (13) Price, S. L. Why don't we find more polymorphs? *Acta Crystallogr., Sect. B: Struct. Sci., Cryst. Eng. Mater.* **2013**, *69*, 313–328.
- (14) Zhabina, A. A.; Nagrimanov, R. N.; Emel'yanenko, V. N.; Solomonov, B. N.; Verevkin, S. P. Nicotinamides: Evaluation of thermochemical experimental properties. *J. Chem. Thermodyn.* **2016**, 103, 69–75.
- (15) Kofler, L.; Kofler, A. Über Molekülverbindungen des Nicotinsäureamids. Ber. Dtsch. Chem. Ges. B 1943, 76, 718–722.
- (16) Kofler, A.; Kolšek, J. Beitrag zur mikroskopischen Identifizierung organischer Stoffe nach L. Kofler. V. *Microchim. Acta* **1971**, 59, 848–874.
- (17) Hino, T.; Ford, J. L.; Powell, M. W. Assessment of nicotinamide polymorphs by differential scanning calorimetry. *Thermochim. Acta* **2001**, 374 (1), 85–92.
- (18) Li, X.; Ou, X.; Wang, B.; Rong, H.; Wang, B.; Chang, C.; Shi, B.; Yu, L.; Lu, M. Rich polymorphism in nicotinamide revealed by melt crystallization and crystal structure prediction. *Commun. Chem.* **2020**, *3*, 152–160.
- (19) Wright, W. B.; King, G. S. D. The crystal structure of nicotinamide. *Acta Crystallogr.* 1954, *7*, 283–288.
- (20) Miwa, Y.; Mizuno, T.; Tsuchida, K.; Taga, T.; Iwata, Y. Experimental charge density and electrostatic potential in nicotinamide. *Acta Crystallogr., Sect. B: Struct. Sci.* 1999, 55, 78–84.
- (21) Jarzembska, K. N.; Hoser, A. A.; Kamiński, R.; Madsen, A. Ø.; Durka, K.; Woźniak, K. Combined experimental and computational studies of pyrazinamide and nicotinamide in the context of crystal engineering and thermodynamics. *Cryst. Growth Des.* **2014**, *14*, 3453–3465.
- (22) Li, J.; Bourne, S. A.; Caira, M. R. New polymorphs of isonicotinamide and nicotinamide. *Chem. Commun.* **2011**, 47, 1530–1532.
- (23) Aakeröy, C. B.; Beatty, A. M.; Helfrich, B. A.; Nieuwenhuyzen, M. Do polymorphic compounds make good cocrystallizing agents? A structural case study that demonstrates the importance of synthon flexibility. *Cryst. Growth Des.* **2003**, *3*, 159–165.
- (24) Eccles, K. S.; Deasy, R. E.; Fábián, L.; Braun, D. E.; Maguire, A. R.; Lawrence, S. E. Expanding the crystal landscape of isonicotinamide: concomitant polymorphism and co-crystallisation. *CrystEng-Comm* **2011**, *13*, 6923–6925.
- (25) Vicatos, A. I.; Caira, M. R. A new polymorph of the common coformer isonicotinamide. *CrystEngComm* **2019**, *21*, 843–849.
- (26) Karthikeyan, K.; Thappa, D. M. Pellagra and skin. *Int. J. Dermatol.* **2002**, *41*, 476–481.
- (27) Elliott, R. B.; Pilcher, C. C.; Stewart, A.; Fergusson, D.; McGregor, M. A. The use of nicotinamide in the prevention of type 1 diabetes. *Ann. N. Y. Acad. Sci.* **1993**, *696*, 333–341.
- (28) Behme, M. T. Nicotinamide and diabetes prevention. *Nutr. Rev.* **1995**, *53*, 137–139.
- (29) Reddy, L. S.; Babu, N. J.; Nangia, A. Carboxamide—pyridine Noxide heterosynthon for crystal engineering and pharmaceutical cocrystals. *Chem. Commun.* **2006**, 1369—1371.
- (30) Wang, L.; Tan, B.; Zhang, H.; Deng, Z. Pharmaceutical cocrystals of diflunisal with nicotinamide or isonicotinamide. *Org. Process Res. Dev.* **2013**, *17*, 1413–1418.
- (31) Godin, A. M.; Ferreira, W. C.; Rocha, L. T. S.; Seniuk, J. G. T.; Paiva, A. L. L.; Merlo, L. A.; Nascimento, E. B.; Bastos, L. F. S.; Coelho, M. M. Antinociceptive and anti-inflammatory activities of nicotinamide and its isomers in different experimental models. *Pharmacol., Biochem. Behav.* **2011**, *99*, 782–788.
- (32) Alba Sorolla, M.; Nierga, C.; José Rodríguez-Colman, M.; Reverter-Branchat, G.; Arenas, A.; Tamarit, J.; Ros, J.; Cabiscol, E. Sir2 is induced by oxidative stress in a yeast model of Huntington

- disease and its activation reduces protein aggregation. Arch. Biochem. Biophys. 2011, 510, 27–34.
- (33) Fokin, V. M.; Zanotto, E. D.; Yuritsyn, N. S.; Schmelzer, J. W. P. Homogeneous crystal nucleation in silicate glasses: a 40 years perspective. *J. Non-Cryst. Solids* **2006**, 352, 2681–2714.
- (34) Yu, L. Inferring thermodynamic stability relationship of polymorphs from melting data. *J. Pharm. Sci.* **1995**, 84, 966–974.
- (35) Shtukenberg, A. G.; Punin, Y. O.; Gunn, E.; Kahr, B. Spherulites. Chem. Rev. 2012, 112, 1805–1838.
- (36) Michel-Lévy, A.; Lacroix, A. Les minéraux des roches; Librairie Polytechnique: Paris, 1888.
- (37) Bernauer, F. Gedrillte Kristalle; Gebruder Bornträger: Berlin, 1929.
- (38) Shtukenberg, A. G.; Zhu, X.; Yang, Y.; Kahr, B. Common occurrence of twisted molecular crystal morphologies from the melt. *Cryst. Growth Des.* **2020**, 20, 6186–6197.
- (39) Caridi, A.; Kulkarni, S. A.; Di Profio, G.; Curcio, E.; ter Horst, J. H. Template-induced nucleation of isonicotinamide polymorphs. *Cryst. Growth Des.* **2014**, *14*, 1135–1141.
- (40) Bhogala, B. R.; Basavoju, S.; Nangia, A. Tape and layer structures in cocrystals of some di- and tricarboxylic acids with 4,4′-bipyridines and isonicotinamide. From binary to ternary cocrystals. *CrystEngComm* **2005**, *7*, 551–562.
- (41) Oswald, I. D. H.; Motherwell, W. D. S.; Parsons, S. Isonicotinamide-formamide (1/1). *Acta Crystallogr., Sect. E: Struct. Rep. Online* **2005**, *61*, o3161–o3163.
- (42) Wang, R.-Y.; Zou, S.-F.; Jiang, B.-Y.; Fan, B.; Hou, M.-F.; Zuo, B.; Wang, X.-P.; Xu, J.-T.; Fan, Z.-Q. A generalized Avrami equation for crystallization kinetics of polymers with concomitant double crystallization processes. *Cryst. Growth Des.* **2017**, *17*, 5908–5917.
- (43) Kirkpatrick, R. J. Crystal growth from the melt: A review. Am. Mineral. 1975, 60, 798-814.
- (44) Huang, C.; Chen, Z.; Gui, Y.; Shi, C.; Zhang, G. G. Z.; Yu, L. Crystal nucleation rates in glass-forming molecular liquids: D-sorbitol, D-arabitol, D-xylitol, and glycerol. *J. Chem. Phys.* **2018**, *149*, 054503.
- (45) Shtukenberg, A. G.; Tan, M.; Vogt-Maranto, L.; Chan, E. J.; Xu, W.; Yang, J.; Tuckerman, M. E.; Hu, C. T.; Kahr, B. Melt crystallization for paracetamol polymorphism. *Cryst. Growth Des.* **2019**, *19*, 4070–4080.
- (46) Chen, S.; Xi, H.; Yu, L. Cross-nucleation between ROY polymorphs. J. Am. Chem. Soc. 2005, 127, 17439–17444.
- (47) Davey, R. J.; Liu, W.; Quayle, M. J.; Tiddy, G. J. T. In situ monitoring of crystallization processes using synchrotron x-ray diffraction: the search for structural precursors. *Cryst. Growth Des.* **2002**, *2*, 269–272.
- (48) Spitaleri, A.; Hunter, C. A.; McCabe, J. F.; Packer, M. J.; Cockroft, S. L. A <sup>1</sup>H NMR study of crystal nucleation in solution. *CrystEngComm* **2004**, *6*, 490–493.
- (49) Hamad, S.; Moon, C.; Catlow, C. R. A.; Hulme, A. T.; Price, S. L. Kinetic insights into the role of the solvent in the polymorphism of 5-fluorouracil from molecular dynamics simulations. *J. Phys. Chem. B* **2006**, *110*, 3323–3329.
- (50) Chen, J.; Trout, B. L. Computational Study of Solvent Effects on the Molecular Self-Assembly of Tetrolic Acid in Solution and Implications for the Polymorph Formed from Crystallization. *J. Phys. Chem. B* **2008**, *112*, 7794–7802.
- (51) Chiarella, R. A.; Gillon, A. L.; Burton, R. C.; Davey, R. J.; Sadiq, G.; Auffret, A.; Cioffi, M.; Hunter, C. A. The nucleation of inosine: the impact of solution chemistry on the appearance of polymorphic and hydrated crystal forms. *Faraday Discuss.* **2007**, *136*, 179–193.
- (52) Chen, D.; Sun, Q.; Huang, W.; Yang, B.-S. Diverse Solvent Selection for Polymorph Landscape Investigation Based on Specific API–Solvent Interactions. *Cryst. Growth Des.* **2020**, *20*, 2251–2265.
- (53) Kulkarni, S. A.; McGarrity, E. S.; Meekes, H.; ter Horst, J. H. Isonicotinamide self-association: the link between solvent and polymorph nucleation. *Chem. Commun.* **2012**, *48*, 4983–4985.
- (54) Zeng, Q.; Mukherjee, A.; Müller, P.; Rogers, R. D.; Myerson, A. S. Exploring the role of ionic liquids to tune the polymorphic outcome of organic compounds. *Chem. Sci.* **2018**, *9*, 1510–1520.

(55) Bakiler, M.; Bolukbasi, O.; Yilmaz, A. An experimental and theoretical study of vibrational spectra of picolinamide, nicotinamide, and isonicotinamide. *J. Mol. Struct.* **2007**, *826*, 6–16.

- (56) Akalin, E.; Yilmaz, A.; Akyuz, S. Vibrational analysis of isonicotinamide. *J. Mol. Struct.* **2005**, 744–747, 881–886.
- (57) Akalin, E.; Akyuz, S. Vibrational analysis of free and hydrogen bonded complexes of nicotinamide and picolinamide. *Vib. Spectrosc.* **2006**, *42*, 333–340.
- (58) Rengarajan, G. T.; Enke, D.; Steinhart, M.; Beiner, M. Size-dependent growth of polymorphs in nanopores and Ostwald's step rule of stages. *Phys. Chem. Chem. Phys.* **2011**, *13*, 21367–21374.
- (59) Digilov, R. M. Semi-empirical model for prediction of crystal—melt interfacial tension. *Surf. Sci.* **2004**, *555*, 68–74.
- (60) Tao, J.; Yu, L. Kinetics of cross-nucleation between polymorphs. J. Phys. Chem. B 2006, 110, 7098-7101.
- (61) Tao, J.; Jones, K. J.; Yu, L. Cross-Nucleation between D-Mannitol Polymorphs in Seeded Crystallization. *Cryst. Growth Des.* **2007**, *7*, 2410–2414.
- (62) Desgranges, C.; Delhommelle, J. Molecular simulation of cross-nucleation between polymorphs. *J. Phys. Chem. B* **2007**, *111*, 1465–1469